ACSNANO

www.acsnano.org

ARTICLE

Echinacoside-Zinc Nanomaterial Inhibits Skin Glycation by Suppressing the Transcriptional Activation of the Receptor for Advanced Glycation End-Products

Jingxia Han, Yu Sun, Ting Wu, Xiaohui Hou, Shaoting Zheng, Haohao Zhang, Tingting Lin,* Huijuan Liu,* and Tao Sun*

Cite This: *ACS Nano* 2023, 17, 14123−14135

Read Online

ACCESS | Metrics & More | Article Recommendations | Supporting Information

ABSTRACT: **Glycation is a nonenzymatically catalyzed spontaneous reaction that eventually leads to the formation of advanced glycation end-products (AGEs), which can bind to the receptor for AGEs (RAGE). The consequences are oxidative damage, an inflammatory response, and aging. In this work, we synthesized echinacoside-zinc coordination polymers (ECH-Zn) by using the coordination interaction between the catechol group of ECH and zinc ions. ECH-Zn was further wrapped with hyaluronic acid/poly (ethylenimine) (HA-PEI) to obtain spherical nanoparticle polymers of HA-PEI-coated ECH-Zn (PPZn). PPZn can enhance the uptake and utilization of ECH-Zn and also have a better antiglycation effect in the skin under the effect of promoting transdermal absorption of HA-PEI. Mechanistic studies at the cellular level showed that MDM2 can interact with STAT2 to form a transcriptional complex and thus promote RAGE transcriptional activation. *In vitro* and *in vivo* studies revealed that PPZn can decrease the expression and inhibit the interaction of the MDM2/STAT2 complex. It inhibited the function of the MDM2/STAT2 complex and suppressed the transcriptional activation of RAGE, thereby exerting antiglycation effects. In conclusion, this work provides a nanomaterial and elucidated a mechanism of anti-skin glycation.**

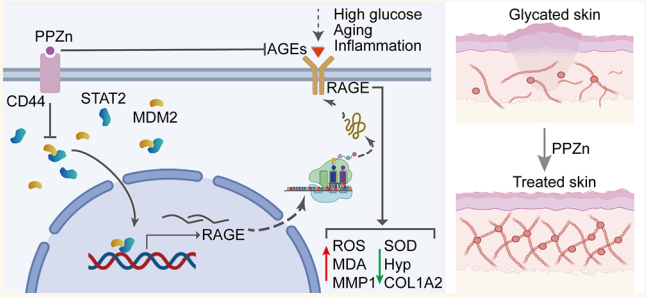

KEYWORDS: *echinacoside, glycation, RAGE, MDM2, STAT2*

INTRODUCTION

Glycation is a nonenzymatic spontaneous reaction that covalently adds free sugars to the terminal amino groups of proteins, lipids, and nucleic acids to form unstable Schiff bases. The Schiff bases undergo a series of rearrangements and/or fragmentation reactions to generate advanced glycation end-products (AGEs).[1] AGEs are considered organic markers of the glycation process.[2] AGEs also have damaging effects on collagen, elastin, and so on, thereby reducing skin elasticity.[2,3] Glycation can affect the stability and functionality of proteins and may impair the functions of the affected cells and tissues, which is one of the mechanisms involved in skin aging.[4,5]

AGEs cause the activation of various signaling pathways triggered by a series of receptors, and the receptor for AGEs (RAGE) is one of the most classical receptors for AGEs.[6,7] RAGE, a member of the immunoglobulin superfamily, was initially isolated from bovine lung in 1992 and accordingly named for acting as a cell surface receptor for AGEs.[8] RAGE, a multiligand pattern-recognition receptor, interacts with various acidic ligands such as AGEs, high-mobility groups box1 (HMGB1), and S100s.[9] RAGE has been implicated in major inflammatory disease states and is significantly upregulated in chronic inflammation.[10] Ligand−RAGE binding affects the initiation and activation of multiple downstream signaling pathways, thereby mediating oxidative stress, inflammatory responses, aging, cancer, and so on.[4,11−13] For example, RAGE ligation activates the proinflammatory transcription factor (TF) NF-κB and sustains the activation of NF-κB, leading to upregulation of RAGE with a positive feed-forward loop that

Received: May 26, 2023
Accepted: June 28, 2023
Published: July 5, 2023

https://doi.org/10.1021/acsnano.3c04726
ACS Nano 2023, 17, 14123−14135

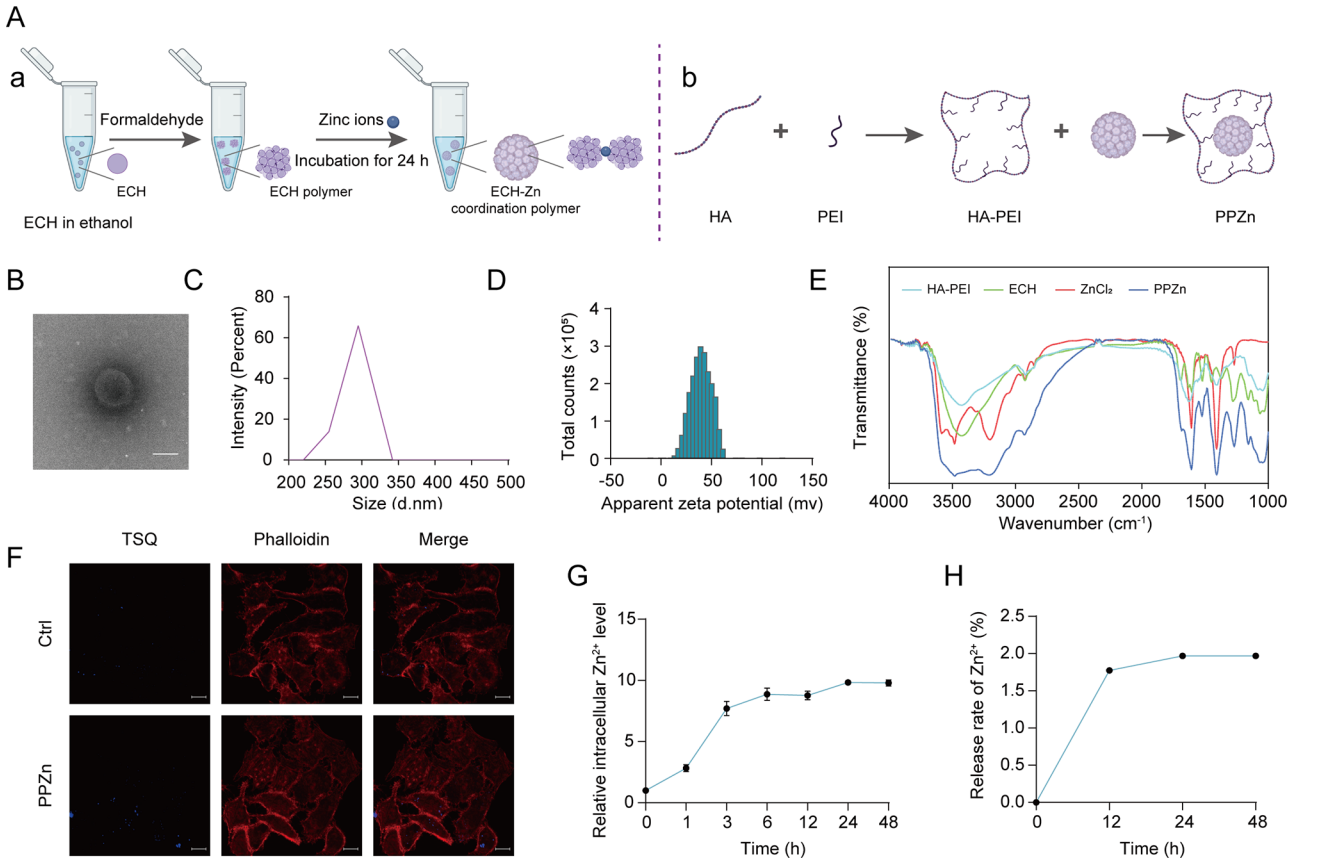

Figure 1. Preparation and characterization of PPZn. (A) Flowchart of PPZn preparation. (B) Morphological detection of PPZn with cryo-TEM. Scale bar, 200 nm. (C) Size measurement of PPZn with NanoSight. (D) Zeta potentials of PPZn. (E) IR spectra of HA-PEI, ECH, $ZnCl_2$, and PPZn. (F) Representative images of Zn^{2+} TSQ staining after the indicated treatment for 24 h. Scale bar, 10 μm. (G) Trend of Zn^{2+} with time detected using a microplate reader. (H) Release of Zn^{2+} as determined by ICP-MS.

further ensures signal maintenance and amplification.[11] Therefore, identifying molecules that can decrease glycation or repress RAGE synthesis is a promising strategy to slow the progression of aging and inflammation, including that in the skin.

The dried succulent stem of *Cistanche* herba is a component of traditional Chinese medicine for treating diabetes, and its antidiabetic activity is further being uncovered as research deepens.[14,15] Natural polyphenolic compounds that have been reported to have strong antioxidant activity.[16] Echinacoside (ECH), a polyphenol isolated from *Cistanche* herba, exerts various effects such as antioxidation, anti-inflammatory, free radical scavenging, anticancer, neuroprotection, osteoprotection, and so on.[17−20] Kong *et al.* evaluated the antioxidant, anti-inflammatory, and protective effects of *Cistanche* herba extract and found that ECH can improve blood sugar levels, insulin resistance, leptin resistance, and lipid peroxidation in diabetic rats.[21] Morikawa *et al.* further demonstrated that ECH significantly improves glucose tolerance in starch-loaded mice without inducing significant changes in body weight or food intake.[22] However, its effect on skin glycation and the specific mechanisms involved are unknown.

Plant polyphenols contain catechol or galloyl groups, so they have strong chelating ability with various metal ions.[23] The metal-polyphenol network (MPN) formed by coordination interactions between metals and phenols exhibits strong potential in various biomedical applications, such as drug delivery, disease treatment, and bioimaging.[24,25] ECH is a natural polyphenol compound with two catechol groups, and we took advantage of this feature to chelate it with zinc ions and form ECH-Zn coordination polymers.

Herein, the role of ECH-Zn in skin glycation was investigated. We synthesized the ECH-Zn ligand polymer and then cross-linked it with hyaluronic acid/poly (ethylenimine) (HA-PEI) to form a nanocomplex named PPZn. Then, we elucidated the mechanism by which PPZn exerts its antiglycation effect by regulating RAGE.

RESULTS

Preparation and Characterization of PPZn. First, we prepared ECH-Zn coordination polymers using the coordination of the catechol group of ECH with zinc ions (Figure 1A−a). Second, we prepared polymers of PPZn by using HA-PEI-wrapped polymers (Figure 1A−b). PPZn was further characterized. Cryo-transmission electron microscopy (cryo-TEM) images demonstrated the morphology of PPZn, which was subspherical (Figure 1B). NanoSight analysis showed that PPZn was around 300 nm (Figure 1C), and its zeta potential was around 40 mV (Figure 1D), indicating good stability. Furthermore, we obtained the infrared (IR) spectra of HA-PEI, ECH, $ZnCl_2$, and PPZn. Results showed that HA-PEI, ECH, and $ZnCl_2$ were successfully fused (Figure 1E). These results indicated that PPZn was a spherical nanoparticle about 300 nm in size, was homogeneous, and had good stability. We then explored whether Zn^{2+} and ECH in PPZn were released into the cells. Cellular staining was performed with the Zn^{2+}-specific

https://doi.org/10.1021/acsnano.3c04726
ACS Nano 2023, 17, 14123−14135

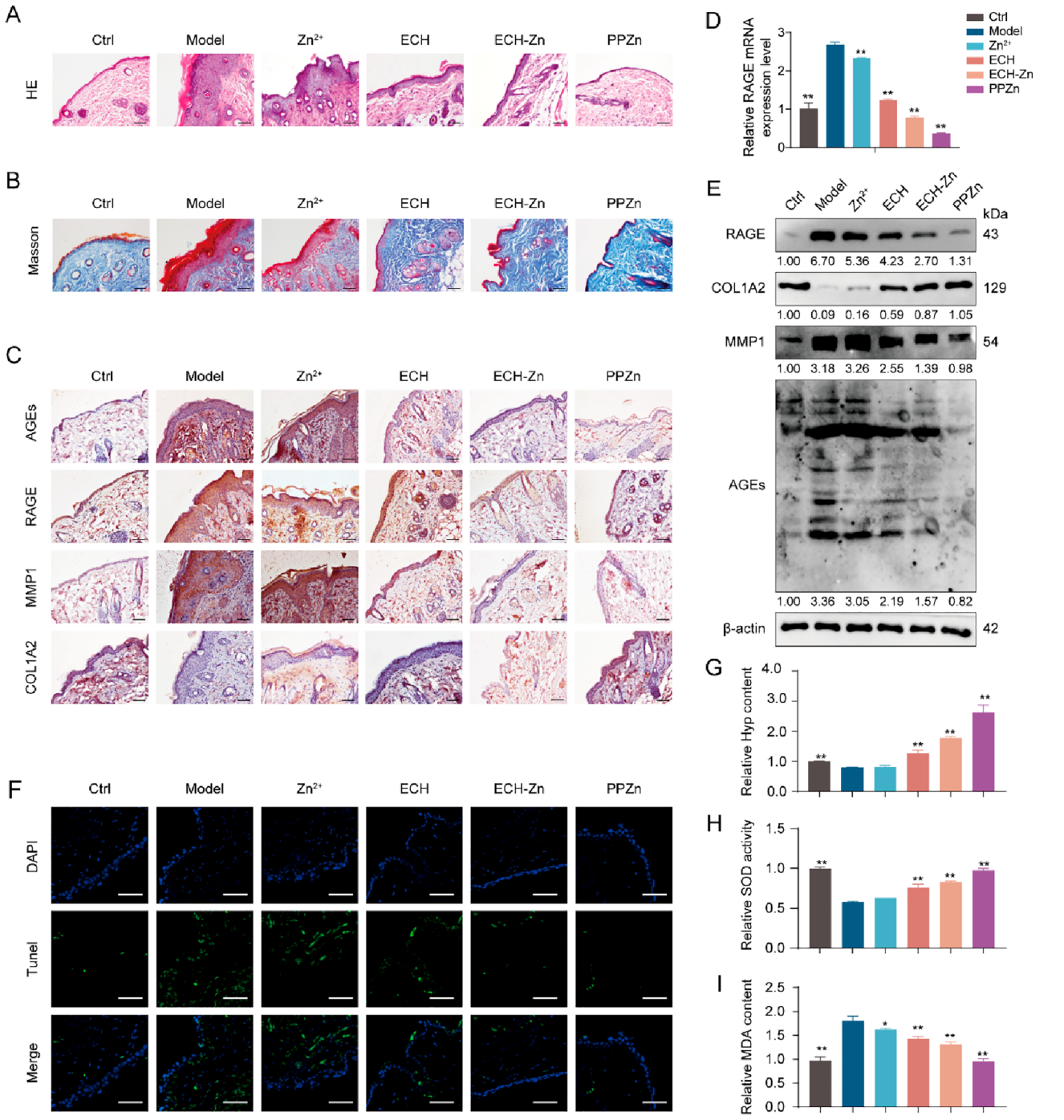

Figure 2. PPZn exerted anti-antiglycan in glycated model mouse skin. (A–C) Representative images of immunohistochemical (IHC) staining (A–a), HE staining (B–a), and Masson staining (C–a) of mouse skin tissue after the indicated treatment. The statistical results of the IHC staining index (A–b), epidermal thickness (B–b), and collagen density (C–b) are shown on the right. Scale bar, 50 μm. (D) qRT-PCR detection of RAGE mRNA levels in skin tissues of mice after the indicated treatment. (E) Western blot representative images and quantitative analysis of RAGE, COL1A2, MMP1, AGEs, and β-actin protein levels in skin tissues of mice after the indicated treatment. (F) Representative images of TUNEL staining of mouse skin tissue after the indicated treatment. Scale bar, 50 μm. (G–I) Relative Hyp content (G), SOD activity (H), and MDA concentration (I) in skin tissues of mice after the indicated treatment. All values are presented as the mean ± SD; *P*-values determined by two-sided Student's *t* test. *$P < 0.05$, **$P < 0.01$, compared with the model.

fluorescent dye *N*-(6-methoxy-8-quinolyl)-*p*-toluenesul fonamide (TSQ). Compared with the low-intensity staining of untreated human immortalized keratinocyte (HaCaT) cells, PPZn-treated cells showed a generalized increase in blue fluorescence with prominent staining of the cytoskeleton stained with phalloidin, suggesting that Zn^{2+} originated from the particle remnants concentrated in the cells (Figure 1F). Meanwhile, Zn^{2+} labeled with TSQ was monitored for 48 h after the addition of PPZn at 334 and 485 nm excitation and emission wavelengths, respectively. Results showed that Zn^{2+} was gradually released over time, and the release level stabilized after 24 h (Figure 1G). Only 1.97% of Zn^{2+} was

https://doi.org/10.1021/acsnano.3c04726
ACS Nano 2023, 17, 14123–14135

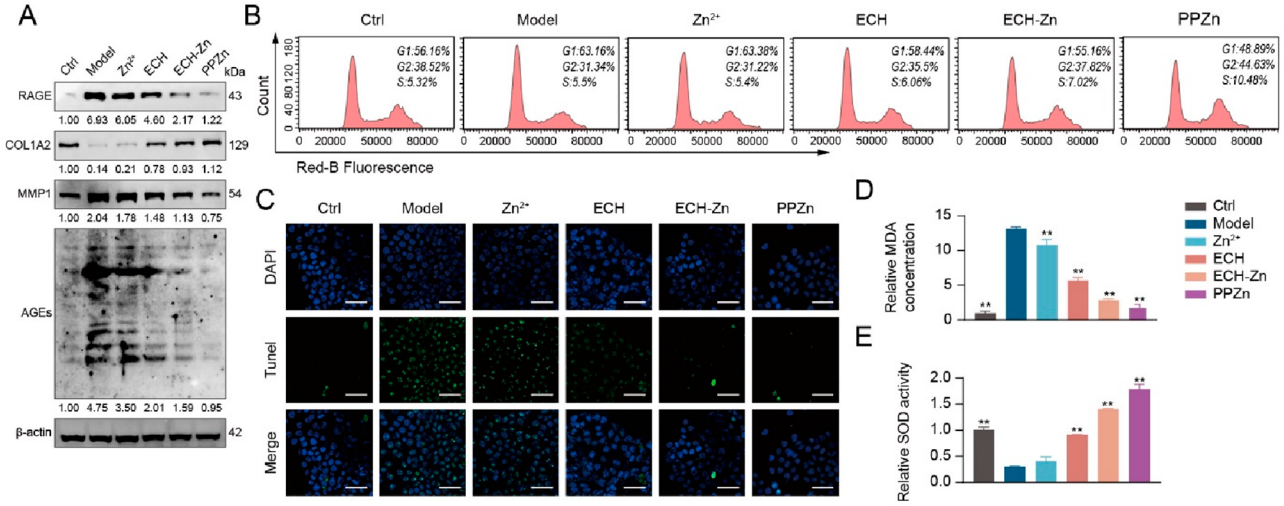

Figure 3. PPZn exerted antiglycation effects in HaCaT cells. (A) Western blot representative images and quantitative analysis of RAGE, COL1A2, MMP1, AGEs, and β-actin protein levels in HaCaT cells after the indicated treatment. (B) Cell cycle was determined by flow cytometry in HaCaT cells after the indicated treatment. (C) Representative images of TUNEL staining of HaCaT cells after the indicated treatment. Scale bar, 50 μm. (D, E) Relative MDA concentration (D) and SOD activity (E) in HaCaT cells after the indicated treatment. All values are presented as the mean ± SD; *P*-values determined by two-sided Student's *t* test. *$P < 0.05$, **$P < 0.01$, compared with the model.

released from PPZn (Figure 1H), whereas ECH was not released significantly. Overall, ECH-Zn in PPZn was efficiently internalized by HaCaT cells and remained in the cells.

ECH and PPZn Exerted Antiglycation Effects in a Mouse Skin Glycation Model and BSA-MGO System *in Vitro*. We established a high-fat diet and D-galactose-induced skin glycation model in mice to demonstrate the effect of PPZn *in vivo*. Prior to animal experiments, cellular-level qRT-PCR screening showed that HA-PEI as a delivery vehicle had no significant effect on RAGE, MMP1, and COL1A2 mRNA levels in the cellular glycation model (Figure S1). Thus, HA-PEI was not included in the subsequent experimental subgroups. RAGE significantly prolonged the inflammatory process. Pro-inflammatory factors were activated, and inflammation resulted in hypertrophic epidermis through the RAGE-induced pathway.[26] HE staining results showed that the epidermal thickness of mice in the control group was 8.14 ± 1.26 μm, whereas that of mice in the model group reached 137.41 ± 6.19 μm. After ECH, ECH-Zn, and PPZn treatment, the levels decreased to 33.05 ± 2.99, 23.77 ± 3.29, and 8.22 ± 2.97 μm, respectively. The epidermal thickness was 132.24 ± 7.07 μm in the Zn^{2+} group, which had no significant ameliorating effect on the inflammatory epidermal thickening caused by glycation. PPZn treatment was the optimum treatment and greatly improved the epidermal thickening to near normal levels (Figure 2A). Results of Masson staining also showed that the loss of skin collagen fibers caused by glycation was greatly improved after ECH-Zn and PPZn treatment, with PPZn being more effective (Figure 2B). The mRNA expression level of RAGE significantly increased in the skin of mice in the model group compared with the control group. The mRNA expression levels of RAGE were reduced to different degrees after different drug treatments, with the optimum effect in the PPZn group, followed by ECH-Zn (Figures 2D and S2A). Glycation triggers skin aging, and MMP1 and type I collagen are markers of aging.[27,28] COL1A2 antibody is used to detect type I collagen. Accordingly, we examined the expressions of AGEs, RAGE, MMP1, and COL1A2 in the skin of mice after different treatments with Western blot and immunohistochemical (IHC) staining. The IHC staining was scored by combining the staining area with the staining intensity. Results showed that the expression levels of AGEs, RAGE, and MMP1 were significantly upregulated in the model group compared with the control, whereas the expression of COL1A2 was downregulated. After treatment with ECH, ECH-Zn, and PPZn, the expression levels of AGEs, RAGE, and MMP1 were downregulated to different degrees. The expression of COL1A2 was upregulated in the PPZn group compared to the model group, with the optimum effect in the PPZn group, followed by ECH-Zn. Meanwhile, Zn^{2+} had a slight inhibitory effect on RAGE, and it had no significant effect on AGEs, MMP1, and COL1A2 (Figures 2C,E and S2B,C).

The process of glycation is often accompanied by apoptosis. Thus, TUNEL fluorescence staining of tissue was performed to observe the apoptosis of skin cells in glycated mice before and after treatment. Glycation-induced apoptosis was significantly inhibited by ECH-Zn and PPZn, with PPZn being more effective (Figure 2F). The levels of hydroxyproline (Hyp), malondialdehyde (MDA), and superoxide dismutase (SOD) in mouse skin were then examined. Hyp is one of the amino acids specific to collagen, and its level can indirectly reflect the change of collagen content in the dermis and thus characterize the degree of skin glycation.[29] MDA content can reflect the rate and intensity of lipid peroxidation in the body, and it also indirectly reflects the degree of peroxidative damage. SOD is a free-radical scavenger and plays an important role in the antioxidant defense system of the skin.[30] Hyp assay results showed that the Hyp content in the skin of glycated mice significantly decreased. Compared with the control and Zn^{2+} groups, the Hyp content was significantly restored after treatment with ECH-Zn and PPZn, and the effect of PPZn was better (Figure 2G). The results of MDA and ROS analyses showed that PPZn can alleviate the glycation-induced MDA accumulation and restore SOD activity, and the effect was better than that of ECH-Zn (Figure 2H,I). Therefore, ECH-Zn and PPZn can effectively inhibit skin glycation and improve the resulting skin inflammation and aging in mice, and the effect of PPZn was better.

https://doi.org/10.1021/acsnano.3c04726
ACS Nano 2023, 17, 14123−14135

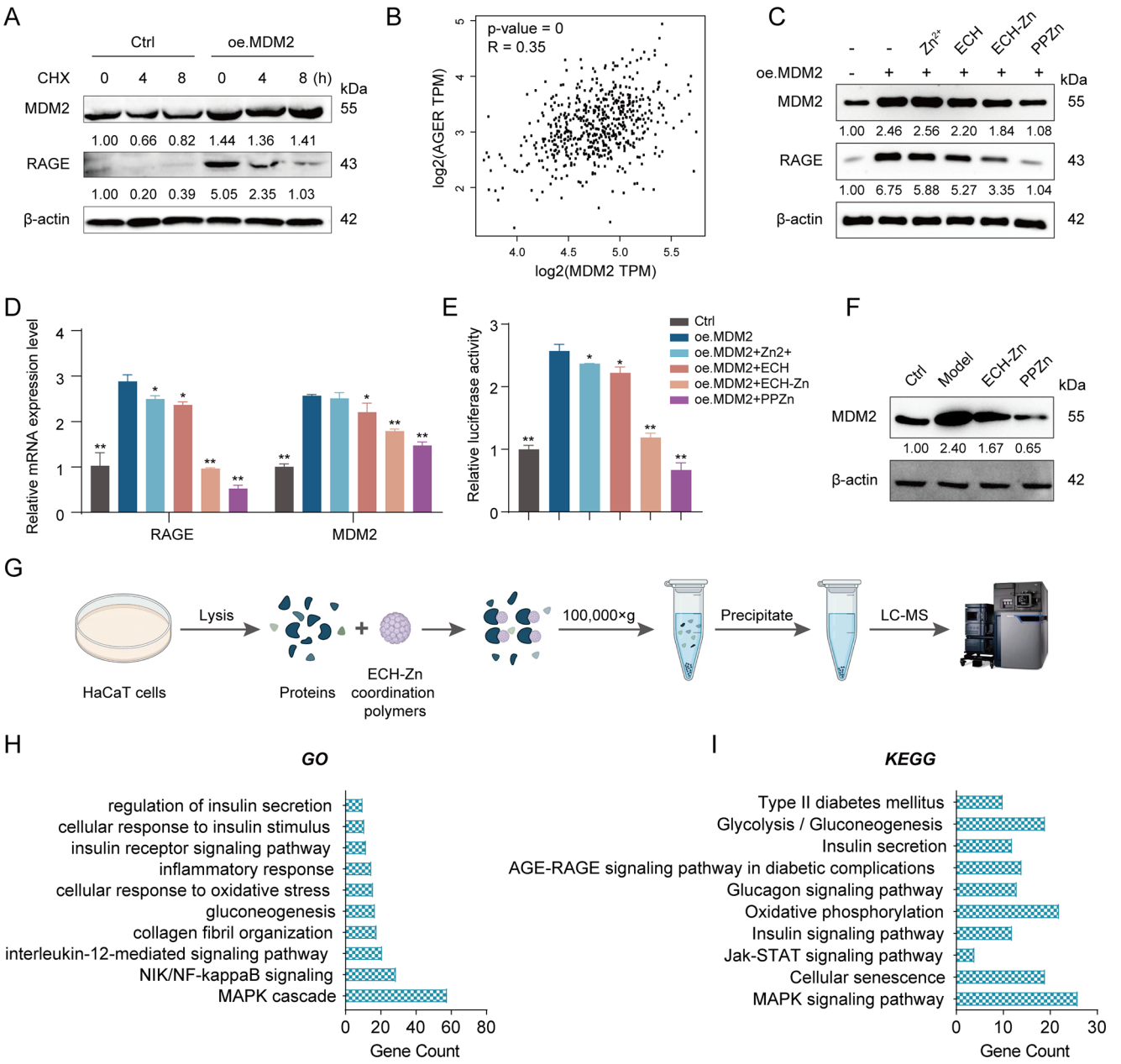

Figure 4. PPZn inhibited RAGE transcriptional activation via MDM2. (A) CHX chase assay for the half-life of RAGE. Western blot representative images and quantitative analysis of MDM2, RAGE, and *β*-actin protein levels in HaCaT cells after the indicated treatment. (B) Correlation analysis between *MDM2* and *AGER* in skin was performed using the GEPIA2 web server. (C) Western blot representative images and quantitative analysis of MDM2, RAGE, and *β*-actin protein levels in HaCaT cells after the indicated treatment. (D) qRT-PCR detection of RAGE and MDM2 mRNA levels in HaCaT cells after the indicated treatment. (E) Relative luciferase activity of RAGE promoter in HaCaT cells after the indicated treatment by dual luciferase reporter gene assay. (F) Western blot representative images and quantitative analysis of MDM2, and *β*-actin protein levels in HaCaT cells after the indicated treatment. (G) Flowchart of SM pulldown. (H, I) GO (H) and KEGG (I) enrichment analysis results of SM pulldown-enriched proteins. All values are presented as the mean ± SD; *P*-values determined by two-sided Student's *t* test. **P* < 0.05, ***P* < 0.01, compared with oe. MDM2.

Methylglyoxal (MGO), an important precursor of AGEs, is one of the most effective and prevalent glycation agents *in vivo*, and its removal is one of the most effective methods to inhibit AGE formation.[31] HA-PEI is a carrier system for the intracellular delivery of drugs and does not exert antiglycation effects (Figure S1). Thus, we used ECH-Zn in experiments *in vitro*. A BSA-MGO incubation system was established to study the effects of Zn^{2+}, ECH, and ECH-Zn on MGO-mediated glycation in AGEs and DNA damage *in vitro*. Results showed that the fluorescence intensity of AGEs of the model group gradually increased with prolonged incubation time from 0 to 7 days compared with that of the control group, thereby indicating the formation and accumulation of AGEs. However, the fluorescence intensity of AGEs in the ECH and ECH-Zn treatment groups was much lower than that of the model group (Figure S3), thereby indicating that ECH and ECH-Zn can effectively inhibit AGE production, and ECH-Zn was more effective. Furthermore, DNA damage induced by MGO was detected by DNA gel electrophoresis, and results showed that ECH and ECH-Zn can inhibit DNA damage by glycation

https://doi.org/10.1021/acsnano.3c04726
ACS Nano 2023, 17, 14123−14135

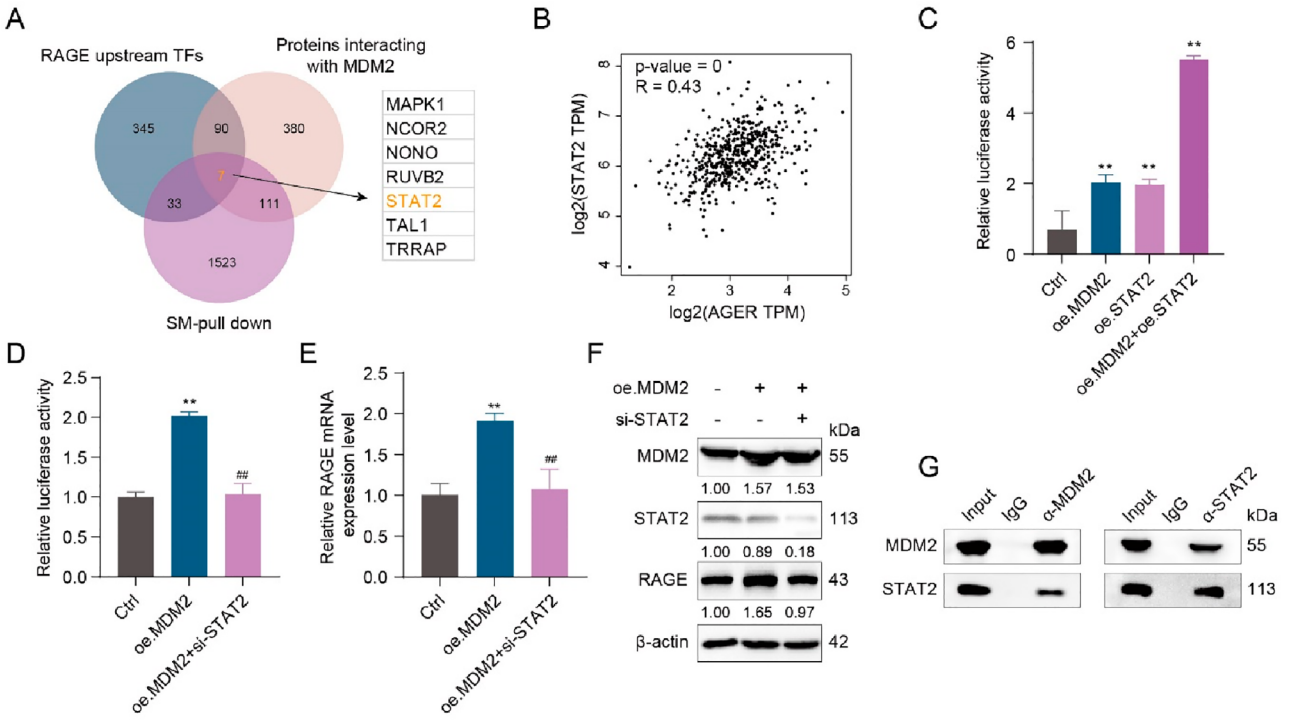

Figure 5. MDM2 formed a transcriptional complex by interacting with STAT2 to promote the transcriptional activation of RAGE. (A) Results of screening for MDM2 interacting transcription factors by Venn diagram. (B) Correlation analysis between *STAT2* and *AGER* in the skin was performed using the GEPIA2 web server. (C, D) Relative luciferase activity of a RAGE promoter in HaCaT cells after the indicated treatment by a dual luciferase reporter gene assay. (E) qRT-PCR detection of RAGE mRNA levels in HaCaT cells after the indicated treatment. (F) Western blot representative images and quantitative analysis of MDM2, STAT2, RAGE, and *β*-actin protein levels in HaCaT cells after the indicated treatment. (G) Co-IP assays in HEK-293T cells after the indicated treatment. All values are presented as the mean ± SD; *P*-values determined by two-sided Student's *t* test. $^{**}P < 0.01$, compared with the control; $^{\#\#}P < 0.01$, compared with oe. MDM2.

products. ECH-Zn was more efficient, whereas Zn^{2+} was ineffective (Figure S4).

PPZn Exerted an Antiglycosylation Effect in HaCaT Cells. We performed a series of experiments to verify the antiglycation effects of Zn^{2+}, ECH, ECH-Zn, and PPZn at the cellular level. First, the effects of Zn^{2+}, ECH, and PPZn on HaCaT cell viability were evaluated (Figure S5). Western blot results showed that glycation led to increased AGEs, RAGE, and MMP1 protein levels and a decrease in COL1A2 protein levels in HaCaT cells. Compared with the model, these alterations were reversed by ECH-Zn and PPZn, with PPZn being more effective. Zn^{2+} slightly downregulated RAGE expression, and COL1A2 and MMP1 were not significantly altered (Figure 3A). Cell-cycle examination by PI labeling revealed that ECH-Zn reversed the G0/G1 block caused by glycation and that PPZn increased the level of G2 and S phase on this basis, which had a promoting effect on cell viability (Figures 3B, S4). Meanwhile, TUNEL cell staining showed that ECH, ECH-Zn, and PPZn significantly inhibited apoptosis triggered by glycation, with PPZn having the optimum effect, followed by ECH-Zn (Figure 3C). ECH-Zn and PPZn can also alleviate the glycation-induced MDA production and restore SOD activity, with PPZn being more effective (Figure 3D,E).

PPZn Inhibited RAGE Activity via MDM2. Recently, we focused more on the functions associated with MDM2 ubiquitination. Accordingly, we performed a cycloheximide pulse-chase experiment to determine whether MDM2 can affect RAGE expression and thus glycation via the ubiquitination pathway. Results showed that MDM2 did not trigger the ubiquitination of the RAGE in HaCaT cells. Instead, it increased the expression of RAGE and prolonged the half-life of RAGE (Figure 4A). A positive correlation between MDM2 and RAGE in skin tissues was revealed through analysis using the GEPIA2 database (Figure 4B). Western blot results indicated that MDM2 increased the protein levels of RAGE, whereas ECH-Zn and PPZn decreased the protein expression levels of MDM2 and RAGE. The effect of PPZn was more pronounced (Figure 4C). The mRNA and promoter levels of RAGE were then verified, and results were consistent with those from Western blot (Figure 4D,E). The Western blot results also showed that MDM2 substantially increased in glycated cells. ECH-Zn and PPZn also restored MDM2 to normal levels in glycated cells (Figure 4F). PPZn can inhibit the promoter activity of RAGE and its expression. However, MDM2 was not a TF, so how it was able to regulate the promoter activity of RAGE warranted investigation. Accordingly, we further explored its regulatory mechanism in the next experiments. Because HA-PEI is a carrier system of ECH-Zn, we used ECH-Zn in *in vitro* experiments. The proteins binding to ECH-Zn polymers were obtained by SM pulldown experiments and identified them by MS to investigate the molecular mechanism of ECH-Zn antiglycosylation (Figure 4G). GO and KEGG analyses were performed on the captured proteins to evaluate in detail the biological processes and functions in which ECH-Zn may be involved. Results showed that most of these proteins were associated with processes, such as inflammation, aging, glycation, and diabetes (Figure 4H,I).

MDM2 Formed a Transcriptional Complex by Interacting with STAT2 to Promote the Transcriptional

https://doi.org/10.1021/acsnano.3c04726
ACS Nano 2023, 17, 14123−14135

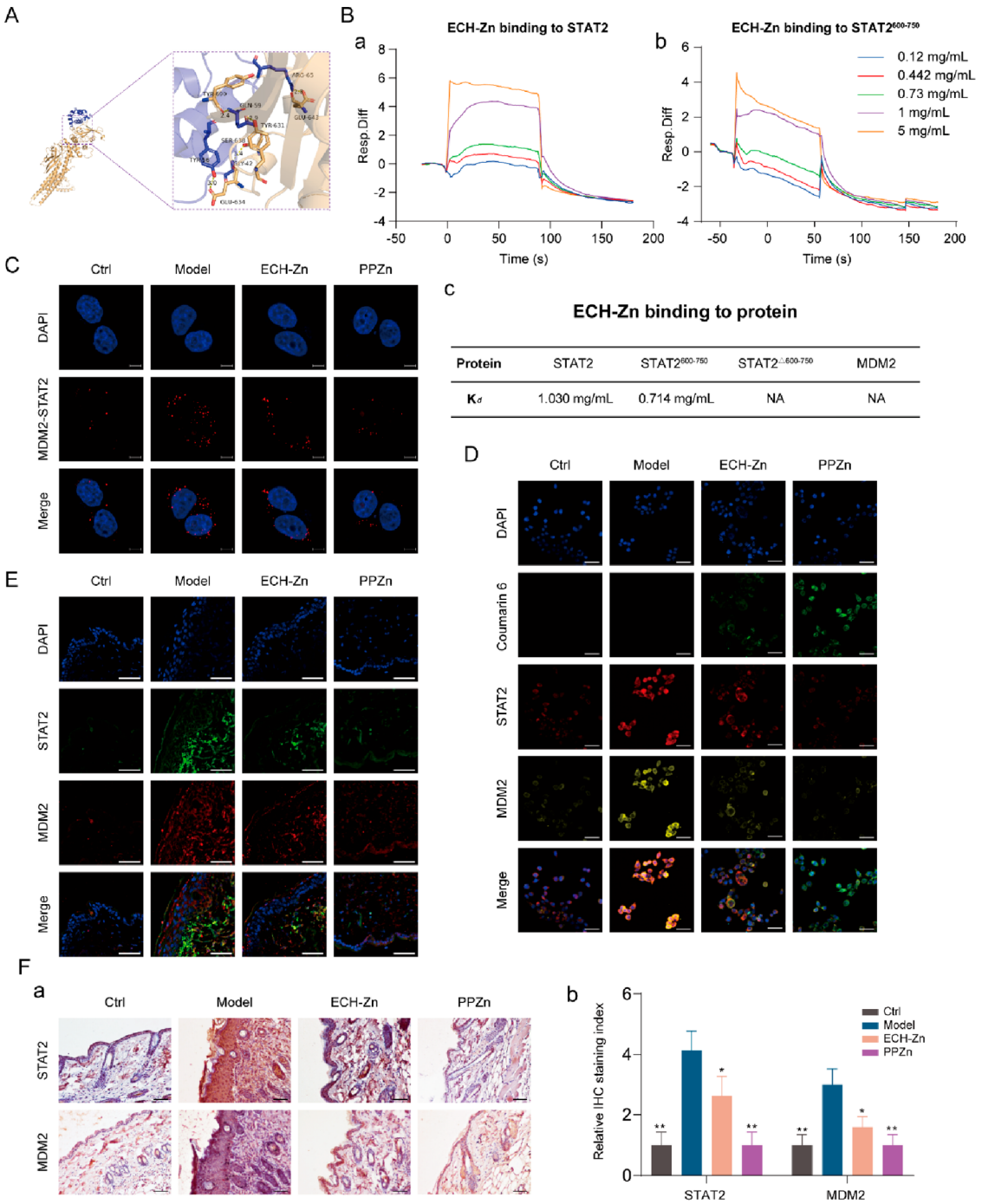

Figure 6. PPZn suppressed RAGE expression by inhibiting the transcriptional complex MDM2/STAT2. (A) Molecular docking of MDM2 (blue) and STAT2 (yellow). (B) Biacore analysis of ECH-Zn bonds to MDM2, STAT2, STAT2$^{600-750}$, and STAT2$^{\Delta 600-750}$. (C) Representative images of PLA assays of HaCaT cells with MDM2 and RAGE interaction after the indicated treatment. Scale bar, 5 μm. (D) ECH-Zn cellular uptake was detected using coumarin-6 fluorescent dye. Representative images of IF in HaCaT cells after the indicated treatment. Scale bar, 50 μm. (E) Representative IF images of mouse skin tissue after the indicated treatment. Scale bar, 50 μm. (F) Representative images of IHC of mouse skin tissue after the indicated treatment are shown in a. Meanwhile, the statistical results of the relative IHC staining index are shown in b. Scale bar, 50 μm. All values are presented as the mean ± SD; *P*-values determined by two-sided Student's *t* test. *$P < 0.05$, **$P < 0.01$, compared with model.

Activation of RAGE. The TFs upstream of RAGE were identified in the ChIP-Base database. The proteins interacting with MDM2 (total score >0.5) were further identified in the GEPIA2 database. A Venn diagram of the two data sets identified above with the SM pulldown data set (peptides ≥5) identified proteins coexisting in three data sets, which were MAPK1, NCOR2, NONO, RUVB2, STAT2, TAL1, and TRRAP (Figure 5A). We correlated each of these seven proteins with RAGE and found that STAT2 correlated best with RAGE in skin tissue (Figures 5B and S6). Thus, we speculated that STAT2 as a TF of RAGE may play an important role in RAGE activation by MDM2. Co-IP and proximity ligation assay (PLA) results suggested an interaction between STAT2 and MDM2 (Figure 5C,D). Overexpression

https://doi.org/10.1021/acsnano.3c04726
ACS Nano 2023, 17, 14123−14135

of either MDM2 or STAT2 alone can increase the transcriptional activity of RAGE, and the level of activation of RAGE greatly increased when both were simultaneously overexpressed (Figure 5E). Accordingly, we hypothesized that MDM2 may promote the transcriptional activation of RAGE through STAT2. Results of the dual luciferase reporter gene assay indicated that MDM2 overexpression alone can promote the transcriptional activity of RAGE. However, when STAT2 was silenced, even MDM2 overexpression failed to promote the transcriptional activation of RAGE (Figure 5F), thereby suggesting that the transcriptional complex formed by MDM2/STAT2 can further promote the transcriptional activation of RAGE. Accordingly, we verified the effects of MDM2 and STAT2 on RAGE expression at the mRNA level and protein level, respectively, and the conclusions drawn were consistent with those of the dual luciferase reporter gene assay (Figure 5G,H). We also verified the effect of STAT2 overexpression plasmid and STAT2 siRNA (Figure S7). In summary, MDM2 can form a transcriptional complex with STAT2 and promote the transcriptional activation of RAGE.

PPZn Suppressed RAGE Expression by Inhibiting the Transcriptional Complex MDM2/STAT2. The detailed binding mode of the MDM2/STAT2 complex is shown in Figure 6A. The residues around the protein−protein interaction interface can form hydrogen bonds. The TYR-56, GLY-42, GLN-59, and ARG-65 of MDM2 formed hydrogen bonds with the GLU-634, SER-638, TYR-631, TYR-690, and LEU-643 of STAT2 with hydrogen-bond lengths of 3.0, 3.4, 2.9, 2.4, and 2.8 Å, respectively. Surface plasmon resonance (SPR) experiments were performed to validate whether ECH-Zn bound to MDM2 and STAT2. Results indicated that ECH-Zn was directly bound to STAT2 in a concentration-dependent manner (K_d = 0.714 mg/mL), whereas no significant binding affinity existed between ECH-Zn and MDM2. Based on the molecular-docking pattern and the results of SPR experiments, we speculated whether ECH-Zn blocked the interaction between STAT2 and MDM2 by binding to the region on STAT2 that interacted with MDM2. We prepared and purified protein truncation, including $STAT2^{600-750}$ and $STAT2^{\Delta 600-750}$. Results showed that ECH-Zn interacted with $STAT2^{600-750}$ but lost activity to $STAT2^{\Delta 600-750}$ (Figure 6B). PLA results revealed that the interaction signal between MDM2 and STAT2 increased after glycation and decreased in the ECH-Zn- or PPZn-treated groups (Figure 6C). Coumarin 6-labeled ECH-Zn was prepared to further verify the effect of ECH-Zn and PPZn. These results suggested that ECH-Zn and PPZn (coumarin-6-labeled ECH-Zn and wrapped with HA-PEI) significantly reduced the expression and colocalization of MDM2 and STAT2 in glycated HaCaT cells. Meanwhile, the fluorescence signal of coumarin-6 was significantly enhanced in the PPZn group, indicating that HA-PEI in PPZn had a stronger delivery effect on ECH-Zn (Figure 6D). Tissue IF and IHC analyses also showed that the expression of MDM2 and STAT2 in the skin of ECH-Zn- and PPZn-treated mice was significantly reduced, and the effect of PPZn was more obvious (Figure 6E,F). In other words, ECH-Zn can reduce the formation and protein expression of the MDM2/STAT2 transcription complex and inhibit the transcriptional activation of RAGE. PPZn strengthened the delivery of ECH-Zn, thereby exerting a stronger anti-skin glycation effect.

DISCUSSION

As a typical active compound isolated from Cistanche herba, ECH has strong anti-inflammatory and antioxidant activities and can improve blood sugar levels.[19,21] Oxidative stress is defined as the overproduction of reactive oxygen species that can trigger oxidative damage leading to cellular oxidative damage, which in turn leads to cancer, neurodegeneration, cardiovascular disease, diabetes, and renal disease.[32−34] Glycation and oxidative damage are closely related *in vivo*, with glycation (glycosylation) disrupting redox homeostasis and oxidative stress driving glycation.[35,36] Thus, redox homeostasis also has a great effect on the treatment of cutaneous glycation. Studies on ECH related to the skin have also focused primarily on antioxidation and skin protection. For example, ECH can promote wound healing,[37] prevent UVB-induced DNA damage and cell apoptosis *in vivo* and *in vitro*,[38] and protect collagen from free radical-induced degradation to prevent skin photodamage.[39] However, few studies have been conducted on the mechanism of ECH inhibiting glycation, and its effects and molecular mechanisms on skin glycation remain unclear. Herein, by establishing cellular and animal glycation models, we found that ECH can reduce the content of AGEs and the expression of RAGE in the skin of glycated mice and exert antiglycation effects. By further establishing protein glycation models *in vitro*, we explored the effects of ECH, ECH-Zn, and PPZn on the inhibition of AGE products and the protection of DNA.

Polyphenols are organic molecules containing phenolic hydroxyl groups that can coordinate with various metal ions to form MPNs. MPNs are used to prepare an important class of nanoparticles containing polyphenols for drug delivery, disease treatment, and bioimaging given their advantages of simple synthesis, flexible structure, pH responsiveness, and good physiological stability.[24,40,41] Among them, Zn^{2+} have been complexed with several organic ligands to develop antidiabetes agents with improved and/or broader pharmacological properties.[42−44] Accordingly, in the present study, we prepared an ECH-Zn based on the formaldehyde-assisted metal−ligand cross-linking strategy.[23] Compared with ECH, ECH-Zn exerted a better therapeutic effect on skin glycation. CD44 is a ubiquitous transmembrane surface receptor.[45] HA, as a natural ligand of CD44, can form a network structure of gels encapsulated on the surface of liposomes and cationic complexes (such as PEI).[46,47] As a cationic polymer carrier, PEI has been widely used for the transmission of nucleic acid-based molecules. However, PEI has significant cytotoxicity and insufficient cell delivery efficiency. Conjugation of HA to PEI reduces the cytotoxic effects of PEI.[48] Notably, our previous work has utilized HA-PEI to achieve highly efficient delivery to cells to exert the efficacy of the contents.[49,50] Therefore, we "coated" the ECH-Zn with the HA-PEI shell to obtain PPZn for enhanced skin drug absorption. Experimental results showed that PPZn had an antiglycation effect superior to that of ECH-Zn and can inhibit RAGE expression by targeting the MDM2/STAT2 transcription complex.

The accumulated AGEs can trigger intracellular signaling pathways by binding to transmembrane receptors, such as RAGE, leading to apoptosis, oxidative stress, inflammatory responses, and so on. RAGE expression in glycated skin cells was significantly reduced by PPZn. MDM2 is an oncogene with major oncogenic activities in cancer. Noncarcinogenic roles for MDM2 have also been identified as research has

https://doi.org/10.1021/acsnano.3c04726
ACS Nano 2023, 17, 14123−14135

progressed, and it is reportedly involved in various disease processes, such as inflammation, autoimmune diseases, diabetes, cardiovascular diseases, and neurodegenerative diseases.[51] Our study found that MDM2 expression was upregulated in glycated skin models and that MDM2 may serve as a potential biomarker and therapeutic target for skin glycation. MDM2 overexpression upregulated RAGE expression in HaCaT cells, and we further identified STAT2 among the binding proteins of MDM2. By analyzing clinical data, we further found that STAT2 was positively correlated with RAGE. STAT2 is a member of the STAT family and is involved in inflammatory reaction and carcinogenesis, as well as other processes.[52] However, whether MDM2/STAT2 regulates the RAGE is unknown. Our study showed that MDM2 can bind to the RAGE promoter by interacting with STAT2 and forming a transcriptional complex, thereby greatly promoting the transcriptional activation of RAGE. In turn, the glycation process in the skin was exacerbated, thereby triggering oxidative damage, inflammatory response, and aging.

CONCLUSIONS

In the current work, we elucidated a mechanism through which MDM2 induces skin glycation by stabilizing STAT2. Zn^{2+}, as an important component of PPZn nanoparticles, stabilized the structure of ECH cross-linked polymers and maintained the biological function of PPZn to exert antiglycosylation effects. The released Zn^{2+} also had a slight antiglycosylation effect but no significant improvement in other skin problems caused by glycosylation. This is also a property of ECH-Zn. The preparation of ECH-Zn integrates the advantages of ECH and Zn and possesses biological functions that ECH and Zn^{2+} do not possess, which can inhibit the formation of the STAT2/MDM2 transcriptional complex, thus inhibiting the transcriptional activation of RAGE and improving the antiglycation effect. And the preparation of PPZn can enhance the uptake and utilization of ECH-Zn based on the target delivery effect of HA-PEI, further enhancing the antiglycosylation effect. The nanomaterial PPZn can deliver the effective antiglycation component ECH-Zn into skin cells with the targeted delivery of surface HA-PEI, reduce the expression of MDM2/STAT2, disrupt its interaction to reduce the level of AGE, and inhibit the transcriptional activation and expression of RAGE. Thus, it can exert antiglycation, anti-inflammatory, antioxidant, and antiaging effects. This study enriched the research theory of skin glycation, and the nanomaterial PPZn can provide an approach for antiglycation therapy.

MATERIALS AND METHODS

Synthesis of the Nanomaterial PPZn. Referring to the synthesis of metal−phenolic coordination spheres,[23] we synthesized PPZn with appropriate modifications. In a typical procedure, F127 (15 mg) was dissolved in a water (3.45 mL) and ethanol (600 μL) mixed solvent. Then, an ammonia solution (37.5 μL) was added, and the solution was stirred for 1 h. After ECH (15 mg) was added to the above solution and its complete dissolution, the formaldehyde solution (28.5 μL) was added. $ZnCl_2$ (3.525 mg) was subsequently added after stirring for 24 h and again for another 24 h. The resulting mixture was centrifuged, washed, and dried to collect the final product of the ECH-Zn coordination polymers. Subsequently, ECH-Zn and HA-PEI were mixed to obtain the final product PPZn.

Material Characterization. PPZn electron microscopy was performed with a cryo-TEM system (Talos F200C, Czechia) to obtain morphology information. PPZn's particle size and zeta potential were detected using a nanoparticle size analyzer (nano ZS, UK). IR spectroscopy was also performed on an infrared spectrometer (TENSOR 37, GER). ICP-MS analysis was conducted with an Agilent ICP-MS 7700x.

Zn^{2+} Release in Cells and Tissues. Cell or tissue samples were lysed and centrifuged for 1 h at 15000*g*, 4 °C, and the supernatant was collected and analyzed by ICP-MS or the Zn^{2+}-specific fluorescent dye TSQ.

Intracellular Zn^{2+} Imaging. HaCaT cells were pretreated in a culture medium containing PPZn for 24 h. After permeabilization and fixation, cells were then rinsed three times with PBS and stained in a PBS solution containing the cytoskeletal marker Phalloidin or TSQ for 30 min. The cells were examined under a confocal microscope (Zeiss LSM 800 with Airyscan).

Surface Plasmon Resonance. SPR analysis was performed using a Biacore X100, Biacore software, and Biacore reagents (GE Healthcare). STAT2, MDM2, $STAT2^{600-750}$, or $STAT2^{\Delta 600-750}$ was separately immobilized on a CM5 sensor based on the manufacturer's instructions (GE Healthcare). For affinity analysis, ECH-Zn was injected at 5, 2.5, 1, 0.73, 0.442, and 0.12 mg/mL concentrations. Each analysis included an empty flow cell to deduct the background signal. Sensor chips were regenerated after each concentration of gp120 using 3 M $MgCl_2$. Association (k_{on}) and dissociation (k_{off}) rate constants were calculated by using a 1:1 Langmuir binding model in Biacore software. The equilibrium dissociation constant (K_d) was calculated from k_{off}/k_{on}.

Cell Culture and Transfection. HaCaT and human embryonic kidney 293T cells (HEK-293T) were purchased from KeyGEN Biotech (Nanjing, China). Cells were maintained in DMEM medium (KeyGEN, China) with appropriate amounts of fetal bovine serum (FBS) and 1% penicillin/streptomycin (KeyGEN, China) in a humidified incubator at 37 °C with 5% CO_2. HaCaT and HEK-293T cells were cultured with 15% and 10% FBS, respectively. HaCaT cells were incubated with 25 mM glucose for 24 h at 37 °C to construct a model of cellular glycation. The Zn^{2+} (1.54 μM), ECH (94 μM), ECH-Zn (ECH 94 μM), and PPZn (ECH 94 μM) were added, respectively. All plasmids or siRNAs were transfected into cells using Lipofectamine 2000 (Invitrogen, USA). Information about plasmids and siRNAs is given in Tables S1 and S2.

Mouse Skin Glycation Model. In an *in vivo* model of D-galactose-induced skin, glycation was established based on a previously reported method.[29] A total of 20 C57BL/6 mice (female, 6−8 weeks old) were used for experiments. The mice were randomly divided into four groups (n = 5): control, model, ECH treatment, and PPZn treatment groups. Mice in model and treatment groups were fed a high-fat diet and subcutaneously injected with 100 mg/kg of D-galactose once daily for 8 weeks. All injections were performed using aseptic techniques, and each injection point was marked with gentian violet. Meanwhile, mice in the treatment group received Zn^{2+} (13.59 μg/kg), ECH (10 mg/kg), ECH-Zn (ECH 10 mg/kg), and PPZn (ECH 10 mg/kg) starting from the fifth week. All mice were euthanized, and skin samples were taken from the injection sites of the dorsal midline of mice. Skin tissues were immediately collected and divided into two parts. One part was quickly frozen in liquid nitrogen and stored at −80 °C, and the other part was fixed in formalin.

BSA-MGO System *in Vitro*. Fluorescence AGE detection: BSA (1 mg/mL), MGO (5 mM), and sodium azide (0.02%) were incubated in potassium phosphate buffer (pH 7.4, 0.2 M). Zn^{2+} (0.77 μM), ECH (50 μM), and ECH-Zn (ECH 50 μM) were added to the above solutions, establishing the control and model groups simultaneously. Samples were incubated at 37 °C, and the fluorescence intensity of the mixture was recorded at 453 and 360 nm emission and excitation wavelengths, respectively, on days 1, 2, 3, 5, and 7. The fluorescence intensity reflected the number of fluorescent AGEs.

DNA damage detection: pGL3-Basic vector (0.1 μg/μL), MGO (100 μM), and ECH or ECH-Zn were incubated in potassium phosphate buffer. Then, the control and model groups were simultaneously established. After incubation at 37 °C for 24 h, the reaction was terminated by adding 10× loading buffer, followed by agarose gel electrophoresis.

https://doi.org/10.1021/acsnano.3c04726
ACS Nano 2023, 17, 14123−14135

Cell-Proliferation Assay. HaCaT cells were grown in 96-well plates. Cells were treated with different concentrations of ECH and PPZn after 24 h. A 10 μL CCK8 solution (ApexBio, USA) was added to each well and incubated with cells at 37 °C in the dark. After 2 h, the 96-well plate was placed into the microplate (Multiskan FC, Thermo) for detection, and the wavelength was set at 450 nm.

Cell Cycle Detection. A cell cycle and apoptosis analysis kit was used to analyze the cell cycle (Yeasen, China). Cells were labeled with propidium iodide (PI). In a typical procedure, samples were fixed with precooled 70% ethanol overnight at 4 °C and then stained with PI containing RNase A for 30 min at 37 °C. Subsequently, detection was performed with a flow cytometer (Guava easyCyte flow cytometers, Luminex), and data were analyzed using FlowJo software.

TUNEL Staining. TUNEL staining in HaCaT cells and mouse skin tissue was performed to assess apoptosis using a TUNEL apoptosis detection kit (Yeasen, China) following the manufacturer's instructions. The nuclei of all cells and apoptotic cells appeared in blue and green, respectively.

RNA Extraction and Real-Time PCR. Total RNA was extracted using a MolPure Cell RNA kit (Yeasen, China). RNA was reverse transcribed into cDNA using cDNA synthesis super mix (Yeasen, China). A SYBR qRT-PCR mix (Zoman Biotechnology, China) was used for transcription with the specific primers. The sequence of primers is given in Table S3. Expression levels were quantified by using the $2^{-\Delta\Delta Ct}$ method with GAPDH as an internal reference.

Western Blot. RIPA lysis buffer with protease inhibitors and a BCA protein assay kit (Thermo, USA) were used to lyse the cells on ice for 30 min and determine the protein content, respectively. Proteins were separated by 8−15% SDS-PAGE and then transferred onto PVDF membranes. After blocking with 5% skim milk powder, the PVDF membranes were incubated with primary antibodies against MDM2 (Proteintech, 1:1000), RAGE (Santa, 1:100), STAT2 (Zenbio, 1:1000), PCNA (Zenbio, 1:5000), MMP1 (Affinity, 1:1000), COL1A2 (Proteintech, 1:5000), AGEs (Abcam, 1:1000), and β-actin (Affinity, 1:10 000) overnight at 4 °C and with HRP-conjugated secondary antibodies for 2 h at room temperature. Imprinting was performed using an ECL reagent (Millipore, USA).

Immunofluorescence (IF). Cells were fixed in 4% paraformaldehyde for 20 min at room temperature and blocked with 5% bovine serum albumin (BSA) and 0.03% Triton X-100 for 50 min. Then, after washing with PBS, cells were incubated with primary antibodies against MDM2 (Proteintech, 1:200), RAGE (Santa, 1:50), and STAT2 (Zenbio, 1:100) at 4 °C overnight and then incubated with Alexa Fluor conjugated secondary antibodies (Thermo, USA) at 37 °C for 1.5 h. Samples were then blocked with an antifading mounting medium with DAPI (Solarbio, China). Finally, observations were performed by using a laser confocal microscope (Zeiss LSM 800 with Airyscan).

Histological Examination of Mouse Skin. All animal procedures were approved by following the guidelines of the Animal Ethics Committee of Tianjin International Joint Academy of Biotechnology and Medicine. Mouse dorsal skin tissues were fixed in formalin for 72 h, embedded in paraffin, and cut into 4-μm-thin sections. Afterward, modified HE stain (Solarbio, China) and modified Masson's trichrome stain kits (Solarbio, China) were used for HE and Masson staining following the manufacturer's method, respectively. For IHC assays, skin tissue sections were deparaffinized, incubated in xylene and a graded ethanol series, and treated with 3% H_2O_2 to block endogenous peroxidase activity. Subsequently, antigen repair with a microwave oven was performed in a sodium citrate antigen repair solution. After being blocked, samples were then incubated with primary antibodies against MDM2 (Proteintech, 1:200), RAGE (Santa, 1:50), STAT2 (Zenbio, 1:100), MMP1 (Affinity, 1:100), COL1A2 (Proteintech, 1:100), and AGEs (Abcam, 1:100) at 4 °C overnight. After PBS washing, an HRP-polymer anti-mouse/rabbit IHC kit (Maixin Biotech, China) was used to incubate the skin tissue at room temperature. A DAB kit (Maixin Biotech, China) and hematoxylin were used for color development and restaining, respectively. The tissue was dehydrated and covered with glass. For IF on tissue sections, the steps were performed before primary antibody treatment as in the step of IHC (without 3% H_2O_2 treatment), followed by the step of IF on cells.

Detection of Oxidative or Senescence Markers. A lipid peroxidation MDA assay kit (Beyotime, China) was used to determine the levels of MDA based on the manufacturer's methods. A Cu/Zn-SOD and Mn-SOD assay kit with WST-8 (Beyotime, China) was used to detect SOD activity. A ROS assay kit (Beyotime, China) was used to determine the ROS levels. A Hyp content assay kit (Beyotime, China) was used to determine the Hyp content.

SM Pulldown. HaCaT cells were lysed with IP lysis buffer (Beyotime, China) containing protease inhibitors. Cell extracts were incubated with ECH-Zn for 24 h at 4 °C. The precipitates were collected by centrifugation, washed, and boiled by adding loading buffer. Proteins were separated by SDS-PAGE electrophoresis followed by silver staining using a rapid silver staining kit (Beyotime, China). Protein bands were collected for in-gel digestion and analyzed by LC-MS/MS.

Proximity Ligation Assay. PLA was used to detect the interaction between MDM2 and STAT2 proteins based on the manufacturer's methods of the Duolink kit (Sigma, USA). In a typical procedure, HaCaT cells were seeded onto glass slides with different treatments. Then, HaCaT cells were washed and blocked before incubation with primary antibodies against MDM2 (Proteintech, 1:200) and STAT2 (Zenbio, 1:100) at 4 °C overnight. After washing, the HaCaT cells were incubated with PLA probes for 1 h at 37 °C, followed by ligation and amplification. DAPI was further used to stain the nucleus. Finally, observations were performed using a laser confocal microscope (Zeiss LSM 800 with Airyscan).

Co-immunoprecipitation (Co-IP). Protein A/G beads were incubated with MDM2 antibody, STAT2 antibody, or IgG for 8 h each to obtain complexes. Total proteins were extracted from HEK-293T cells and incubated with complexes overnight at 4 °C. After unbound proteins were washed away, samples were boiled at 100 °C for 10 min. CoIP samples were analyzed by Western blot. IgG antibody served as a negative control.

Luciferase Reporter Assay. The dual luciferase reporter assay was used to determine whether MDM2 or STAT2 can interact with the RAGE promoter fragment. In a typical procedure, the promoter fragment of the RAGE was cloned into the PGL3-Basic plasmid to construct the RAGE promoter plasmid. The pcDNA3.1-STAT2 plasmid or pcDNA3.1-MDM2 plasmid to be detected was co-transfected with the RAGE promoter plasmid and PRL-TK plasmid to HEK-293T cells. After 48 h of transfection, luciferase activity was detected using a Dual-Lumi luciferase assay kit (Beyotime, China) following the manufacturer's instructions.

Molecular Docking. Rigid protein−protein docking (Zdock) was performed between MDM2 and STAT2 to study their relationships. The PDB format of the protein structural domain was downloaded from the PDB Database. The protein structure was imported into Pymol 2.3.0 to remove crystalline water, SMs, *etc.*, and Zdock was used to dock MDM2 and STAT2.

Statistical Analysis. All final data are presented as the mean ± SD. The differences between groups were assessed through a two-sided Student's *t* test. Significance criteria were set as $^*P < 0.05$ and $^{**}P < 0.01$.

ASSOCIATED CONTENT

Supporting Information

The Supporting Information is available free of charge at https://pubs.acs.org/doi/10.1021/acsnano.3c04726.

qRT-PCR detection; statistical graph of skin epidermal thickness, collagen ratio, and relative IHC staining index in mice; effects of Zn^{2+}, ECH, and ECH-Zn on the formation of AGEs in the BSA-MGO system; electropherogram of MGO-damaged DNA inhibited by Zn^{2+}, ECH, and ECH-Zn; CCK8 results for ECH, Zn^{2+}, and PPZn; correlation analysis between *MAPK1*, *NCOR2*, *NONO*, *RUVBL2*, *TAL1* or *TRRAP*, and *AGER* in skin;

https://doi.org/10.1021/acsnano.3c04726
ACS Nano 2023, 17, 14123−14135

Western blot analysis of STAT2, RAGE, and β-actin protein levels in HaCaT cells after indicated treatment; plasmid information; sequences of siRNA; sequences of qRT-PCR primers (PDF)

AUTHOR INFORMATION

Corresponding Authors

Tao Sun − *State Key Laboratory of Medicinal Chemical Biology and College of Pharmacy, Nankai University, Tianjin 300350, China*; Email: tao.sun@nankai.edu.cn

Huijuan Liu − *State Key Laboratory of Medicinal Chemical Biology and College of Pharmacy, Nankai University, Tianjin 300350, China*; orcid.org/0000-0002-8096-7005; Email: huijuan.liu@nankai.edu.cn

Tingting Lin − *Medical Plastic and Cosmetic Center, Tianjin Branch of National Clinical Research Center for Ocular Disease, Tianjin Medical University Eye Hospital, Tianjin 300384, China*; Email: ltt6123@126.com

Authors

Jingxia Han − *State Key Laboratory of Medicinal Chemical Biology and College of Pharmacy, Nankai University, Tianjin 300350, China*

Yu Sun − *State Key Laboratory of Medicinal Chemical Biology and College of Pharmacy, Nankai University, Tianjin 300350, China; Tianjin Key Laboratory of Molecular Drug Research, Tianjin International Joint Academy of Biomedicine, Tianjin 300457, China*

Ting Wu − *State Key Laboratory of Medicinal Chemical Biology and College of Pharmacy, Nankai University, Tianjin 300350, China*

Xiaohui Hou − *State Key Laboratory of Medicinal Chemical Biology and College of Pharmacy, Nankai University, Tianjin 300350, China*

Shaoting Zheng − *State Key Laboratory of Medicinal Chemical Biology and College of Pharmacy, Nankai University, Tianjin 300350, China*

Haohao Zhang − *State Key Laboratory of Medicinal Chemical Biology and College of Pharmacy, Nankai University, Tianjin 300350, China*

Complete contact information is available at: https://pubs.acs.org/10.1021/acsnano.3c04726

Author Contributions

J.X.H., Y.S., and T.W. contributed equally to this work. T.S., H.J.L., T.T.L., and J.X.H. conceived and designed the experiment. J.X.H., Y.S., X.H.H., and S.T.Z. performed all experiments. T.W. and H.H.Z. analyzed and interpreted the data. J.X.H., Y.S., and T.W. prepared the illustrations and drafted the manuscript. All authors read and approved the final manuscript.

Funding

This work was supported by grants from the National Natural Science Foundation of China (grant nos. 82073205, 82272934, and 82273237); the National Youth Talent Support Program (2020); the Natural Science Foundation of Tianjin (grant nos. 19JCJQJC63200, and 21JCZDJC00930); the Fundamental Research Funds for the Central Universities (grant no. 735-63233164); and China Postdoctoral Science Foundation (grant no. 2021M701778).

Notes

The authors declare no competing financial interest.

ACKNOWLEDGMENTS

We are grateful to the BioRender website (https://biorender.com/) for helping us with the graphing process.

REFERENCES

(1) González, I.; Morales, M. A.; Rojas, A. Polyphenols and AGEs/RAGE axis. Trends and challenges. *Food Research International (Ottawa, Ont.)* **2020**, *129*, 108843.

(2) Perrone, A.; Giovino, A.; Benny, J.; Martinelli, F. Advanced Glycation End Products (AGEs): Biochemistry, Signaling, Analytical Methods, and Epigenetic Effects. *Oxidative medicine and cellular longevity* **2020**, *2020*, 3818196.

(3) Paul, R. G.; Bailey, A. J. Glycation of collagen: the basis of its central role in the late complications of ageing and diabetes. *international journal of biochemistry & cell biology* **1996**, *28* (12), 1297−1310.

(4) Pageon, H.; Zucchi, H.; Pennacchi, P. C.; Asselineau, D. Glycation and Skin Aging. In *Textbook of Aging Skin*; Farage, M. A.; Miller, K. W.; Maibach, H. I., Eds.; Springer Berlin Heidelberg, 2017; pp 1247−1270.

(5) Gomes, R. A.; Oliveira, L. M.; Silva, M.; Ascenso, C.; Quintas, A.; Costa, G.; Coelho, A. V.; Sousa Silva, M.; Ferreira, A. E.; Ponces Freire, A.; et al. Protein glycation *in vivo*: functional and structural effects on yeast enolase. *Biochemical journal* **2008**, *416* (3), 317−326.

(6) Twarda-Clapa, A.; Olczak, A.; Białkowska, A. M.; Koziołkiewicz, M. Advanced Glycation End-Products (AGEs): Formation, Chemistry, Classification, Receptors, and Diseases Related to AGEs. *Cells* **2022**, *11* (8), DOI: 10.3390/cells11081312.

(7) Bierhaus, A.; Hofmann, M. A.; Ziegler, R.; Nawroth, P. P. AGEs and their interaction with AGE-receptors in vascular disease and diabetes mellitus. I. The AGE concept. *Cardiovascular research* **1998**, *37* (3), 586−600.

(8) Neeper, M.; Schmidt, A. M.; Brett, J.; Yan, S. D.; Wang, F.; Pan, Y. C.; Elliston, K.; Stern, D.; Shaw, A. Cloning and expression of a cell surface receptor for advanced glycosylation end products of proteins. *J. Biol. Chem.* **1992**, *267* (21), 14998−15004.

(9) El-Far, A. H.; Sroga, G.; Jaouni, S. K. A.; Mousa, S. A. Role and Mechanisms of RAGE-Ligand Complexes and RAGE-Inhibitors in Cancer Progression. *International journal of molecular sciences* **2020**, *21* (10), DOI: 10.3390/ijms21103613.

(10) Hudson, B. I.; Lippman, M. E. Targeting RAGE Signaling in Inflammatory Disease. *Annual review of medicine* **2018**, *69*, 349−364.

(11) Bierhaus, A.; Humpert, P. M.; Morcos, M.; Wendt, T.; Chavakis, T.; Arnold, B.; Stern, D. M.; Nawroth, P. P. Understanding RAGE, the receptor for advanced glycation end products. *Journal of molecular medicine (Berlin, Germany)* **2005**, *83* (11), 876−886.

(12) Ahmad, S.; Khan, H.; Siddiqui, Z.; Khan, M. Y.; Rehman, S.; Shahab, U.; Godovikova, T.; Silnikov, V. Moinuddin. AGEs, RAGEs and s-RAGE; friend or foe for cancer. *Seminars in cancer biology* **2018**, *49*, 44−55.

(13) Sims, G. P.; Rowe, D. C.; Rietdijk, S. T.; Herbst, R.; Coyle, A. J. HMGB1 and RAGE in inflammation and cancer. *Annual review of immunology* **2010**, *28*, 367−388.

(14) Zhu, K.; Meng, Z.; Tian, Y.; Gu, R.; Xu, Z.; Fang, H.; Liu, W.; Huang, W.; Ding, G.; Xiao, W. Hypoglycemic and hypolipidemic effects of total glycosides of Cistanche tubulosa in diet/streptozotocin-induced diabetic rats. *Journal of ethnopharmacology* **2021**, *276*, 113991.

(15) Xiong, W. T.; Gu, L.; Wang, C.; Sun, H. X.; Liu, X. Anti-hyperglycemic and hypolipidemic effects of Cistanche tubulosa in type 2 diabetic db/db mice. *Journal of ethnopharmacology* **2013**, *150* (3), 935−945.

(16) Siracusa, R.; Scuto, M.; Fusco, R.; Trovato, A.; Ontario, M. L.; Crea, R.; Di Paola, R.; Cuzzocrea, S.; Calabrese, V. Anti-inflammatory and Anti-oxidant Activity of Hidrox((R)) in Rotenone-Induced Parkinson's Disease in Mice. *Antioxidants (Basel)* **2020**, *9* (9), DOI: 10.3390/antiox9090824.

(17) Li, F.; Yang, X.; Yang, Y.; Guo, C.; Zhang, C.; Yang, Z.; Li, P. Antiosteoporotic activity of echinacoside in ovariectomized rats. *Phytomedicine: international journal of phytotherapy and phytopharmacology* **2013**, *20* (6), 549−557.
(18) Zeng, K. W.; Wang, J. K.; Wang, L. C.; Guo, Q.; Liu, T. T.; Wang, F. J.; Feng, N.; Zhang, X. W.; Liao, L. X.; Zhao, M. M.; et al. Small molecule induces mitochondrial fusion for neuroprotection *via* targeting CK2 without affecting its conventional kinase activity. *Signal transduction and targeted therapy* **2021**, *6* (1), 71.
(19) Li, L.; Wan, G.; Han, B.; Zhang, Z. Echinacoside alleviated LPS-induced cell apoptosis and inflammation in rat intestine epithelial cells by inhibiting the mTOR/STAT3 pathway. *Biomedicine & pharmacotherapy = Biomedecine & pharmacotherapie* **2018**, *104*, 622−628.
(20) Shi, S.; Qin, Y.; Chen, D.; Deng, Y.; Yin, J.; Liu, S.; Yu, H.; Huang, H.; Chen, C.; Wu, Y.; et al. Echinacoside (ECH) suppresses proliferation, migration, and invasion of human glioblastoma cells by inhibiting Skp2-triggered epithelial-mesenchymal transition (EMT). *European journal of pharmacology* **2022**, *932*, 175176.
(21) Kong, Z. L.; Johnson, A.; Ko, F. C.; He, J. L.; Cheng, S. C. Effect of Cistanche Tubulosa Extracts on Male Reproductive Function in Streptozotocin−Nicotinamide-Induced Diabetic Rats. *Nutrients* **2018**, *10* (10), DOI: 10.3390/nu10101562.
(22) Morikawa, T.; Ninomiya, K.; Imamura, M.; Akaki, J.; Fujikura, S.; Pan, Y.; Yuan, D.; Yoshikawa, M.; Jia, X.; Li, Z.; et al. Acylated phenylethanoid glycosides, echinacoside and acteoside from Cistanche tubulosa, improve glucose tolerance in mice. *Journal of natural medicines* **2014**, *68* (3), 561−566.
(23) Wei, J.; Wang, G.; Chen, F.; Bai, M.; Liang, Y.; Wang, H.; Zhao, D.; Zhao, Y. Sol-Gel Synthesis of Metal-Phenolic Coordination Spheres and Their Derived Carbon Composites. *Angewandte Chemie (International ed. in English)* **2018**, *57* (31), 9838−9843.
(24) Guo, Y.; Sun, Q.; Wu, F. G.; Dai, Y.; Chen, X. Polyphenol-Containing Nanoparticles: Synthesis, Properties, and Therapeutic Delivery. *Advanced materials (Deerfield Beach, Fla.)* **2021**, *33* (22), No. e2007356.
(25) Chen, J.; Li, J.; Zhou, J.; Lin, Z.; Cavalieri, F.; Czuba-Wojnilowicz, E.; Hu, Y.; Glab, A.; Ju, Y.; Richardson, J. J.; et al. Metal-Phenolic Coatings as a Platform to Trigger Endosomal Escape of Nanoparticles. *ACS Nano* **2019**, *13* (10), 11653−11664.
(26) Wang, L. L.; Zhao, R.; Li, J. Y.; Li, S. S.; Liu, M.; Wang, M.; Zhang, M. Z.; Dong, W. W.; Jiang, S. K.; Zhang, M.; et al. Pharmacological activation of cannabinoid 2 receptor attenuates inflammation, fibrogenesis, and promotes re-epithelialization during skin wound healing. *European journal of pharmacology* **2016**, *786*, 128−136.
(27) Gu, Y.; Han, J.; Jiang, C.; Zhang, Y. Biomarkers, oxidative stress and autophagy in skin aging. *Ageing research reviews* **2020**, *59*, 101036.
(28) Xia, W.; Hammerberg, C.; Li, Y.; He, T.; Quan, T.; Voorhees, J. J.; Fisher, G. J. Expression of catalytically active matrix metalloproteinase-1 in dermal fibroblasts induces collagen fragmentation and functional alterations that resemble aged human skin. *Aging cell* **2013**, *12* (4), 661−671.
(29) Umbayev, B.; Askarova, S.; Almabayeva, A.; Saliev, T.; Masoud, A. R.; Bulanin, D. Galactose-Induced Skin Aging: The Role of Oxidative Stress. *Oxidative medicine and cellular longevity* **2020**, *2020*, 7145656.
(30) Bickers, D. R.; Athar, M. Oxidative stress in the pathogenesis of skin disease. *Journal of investigative dermatology* **2006**, *126* (12), 2565−2575.
(31) Ni, M.; Song, X.; Pan, J.; Gong, D.; Zhang, G. Vitexin Inhibits Protein Glycation through Structural Protection, Methylglyoxal Trapping, and Alteration of Glycation Site. *Journal of agricultural and food chemistry* **2021**, *69* (8), 2462−2476.
(32) Pisoschi, A. M.; Pop, A. The role of antioxidants in the chemistry of oxidative stress: A review. *Eur. J. Med. Chem.* **2015**, *97*, 55−74.
(33) Calabrese, V.; Cornelius, C.; Dinkova-Kostova, A. T.; Calabrese, E. J.; Mattson, M. P. Cellular stress responses, the hormesis paradigm, and vitagenes: novel targets for therapeutic intervention in neurodegenerative disorders. *Antioxid Redox Signal* **2010**, *13* (11), 1763−1811.
(34) Calabrese, V.; Mancuso, C.; Calvani, M.; Rizzarelli, E.; Butterfield, D. A.; Stella, A. M. Nitric oxide in the central nervous system: neuroprotection versus neurotoxicity. *Nat. Rev. Neurosci* **2007**, *8* (10), 766−775.
(35) Calabrese, V.; Guagliano, E.; Sapienza, M.; Mancuso, C.; Butterfield, D. A.; Stella, A. M. Redox regulation of cellular stress response in neurodegenerative disorders. *Ital J. Biochem* **2006**, *55* (3−4), 263−282.
(36) Cardoso Gde, S.; Coelho, P. M. [Schistosoma mansoni: development of worms from cercaria irradiated at the porta system level, in mice]. *Rev. Soc. Bras Med. Trop* **1989**, *22* (4), 199−210.
(37) Speroni, E.; Govoni, P.; Guizzardi, S.; Renzulli, C.; Guerra, M. C. Anti-inflammatory and cicatrizing activity of Echinacea pallida Nutt. root extract. *Journal of ethnopharmacology* **2002**, *79* (2), 265−272.
(38) Zhang, D.; Lu, C.; Yu, Z.; Wang, X.; Yan, L.; Zhang, J.; Li, H.; Wang, J.; Wen, A. Echinacoside Alleviates UVB Irradiation-Mediated Skin Damage *via* Inhibition of Oxidative Stress, DN.A.; Damage,, and Apoptosis. *Oxidative medicine and cellular longevity* **2017**, *2017*, 6851464.
(39) Facino, R. M.; Carini, M.; Aldini, G.; Saibene, L.; Pietta, P.; Mauri, P. Echinacoside and caffeoyl conjugates protect collagen from free radical-induced degradation: a potential use of Echinacea extracts in the prevention of skin photodamage. *Planta medica* **1995**, *61* (6), 510−514.
(40) Liu, T.; Zhang, M.; Liu, W.; Zeng, X.; Song, X.; Yang, X.; Zhang, X.; Feng, J. Metal Ion/Tannic Acid Assembly as a Versatile Photothermal Platform in Engineering Multimodal Nanotheranostics for Advanced Applications. *ACS Nano* **2018**, *12* (4), 3917−3927.
(41) Guo, J.; Ping, Y.; Ejima, H.; Alt, K.; Meissner, M.; Richardson, J. J.; Yan, Y.; Peter, K.; von Elverfeldt, D.; Hagemeyer, C. E.; et al. Engineering multifunctional capsules through the assembly of metal-phenolic networks. *Angewandte Chemie (International ed. in English)* **2014**, *53* (22), 5546−5551.
(42) Chukwuma, C. I.; Mashele, S. S.; Eze, K. C.; Matowane, G. R.; Islam, S. M.; Bonnet, S. L.; Noreljaleel, A. E. M.; Ramorobi, L. M. A comprehensive review on zinc(II) complexes as anti-diabetic agents: The advances, scientific gaps and prospects. *Pharmacological research* **2020**, *155*, 104744.
(43) Abd El-Khalik, S. R.; Nasif, E.; Arakeep, H. M.; Rabah, H. The Prospective Ameliorative Role of Zinc Oxide Nanoparticles in STZ-Induced Diabetic Nephropathy in Rats: Mechanistic Targeting of Autophagy and Regulating Nrf2/TXNIP/NLRP3 Inflammasome Signaling. *Biological trace element research* **2022**, *200* (4), 1677−1687.
(44) Sengani, M.; Chakraborty, S.; Balaji, M. P.; Govindasamy, R.; Alahmadi, T. A.; Al Obaid, S.; Karuppusamy, I.; Lan Chi, N. T.; Brindhadevi, K. V D. R. Anti-diabetic efficacy and selective inhibition of methyl glyoxal, intervention with biogenic Zinc oxide nanoparticle. *Environmental research* **2023**, *216* (Pt 2), 114475.
(45) Bourguignon, L. Y.; Ramez, M.; Gilad, E.; Singleton, P. A.; Man, M. Q.; Crumrine, D. A.; Elias, P. M.; Feingold, K. R. Hyaluronan-CD44 interaction stimulates keratinocyte differentiation, lamellar body formation/secretion, and permeability barrier homeostasis. *Journal of investigative dermatology* **2006**, *126* (6), 1356−1365.
(46) Zhang, Y.; Xia, Q.; Li, Y.; He, Z.; Li, Z.; Guo, T.; Wu, Z.; Feng, N. CD44 Assists the Topical Anti-Psoriatic Efficacy of Curcumin-Loaded Hyaluronan-Modified Ethosomes: A New Strategy for Clustering Drug in Inflammatory Skin. *Theranostics* **2019**, *9* (1), 48−64.
(47) Manca, M. L.; Castangia, I.; Zaru, M.; Nacher, A.; Valenti, D.; Fernandez-Busquets, X.; Fadda, A. M.; Manconi, M. Development of curcumin loaded sodium hyaluronate immobilized vesicles (hyalurosomes) and their potential on skin inflammation and wound restoring. *Biomaterials* **2015**, *71*, 100−109.
(48) Han, S. E.; Kang, H.; Shim, G. Y.; Kim, S. J.; Choi, H. G.; Kim, J.; Hahn, S. K.; Oh, Y. K. Cationic derivatives of biocompatible

hyaluronic acids for delivery of siRNA and antisense oligonucleotides. *J. Drug Target* **2009**, *17* (2), 123−132.
(49) Han, J.; Wu, T.; Jin, J.; Li, Z.; Cheng, W.; Dai, X.; Yang, K.; Zhang, H.; Zhang, Z.; Zhang, H.; et al. Exosome-like nanovesicles derived from Phellinus linteus inhibit Mical2 expression through cross-kingdom regulation and inhibit ultraviolet-induced skin aging. *J. Nanobiotechnol.* **2022**, *20* (1), 455.
(50) Li, Y.; Zhang, H.; Chen, C.; Qiao, K.; Li, Z.; Han, J.; Han, X.; Li, K.; Lai, K.; Liu, N.; et al. Biomimetic Immunosuppressive Exosomes that Inhibit Cytokine Storms Contribute to the Alleviation of Sepsis. *Advanced materials (Deerfield Beach, Fla.)* **2022**, *34* (19), No. e2108476.
(51) Wang, W.; Qin, J. J.; Rajaei, M.; Li, X.; Yu, X.; Hunt, C.; Zhang, R. Targeting MDM2 for novel molecular therapy: Beyond oncology. *Medicinal research reviews* **2020**, *40* (3), 856−880.
(52) Lee, C. J.; An, H. J.; Cho, E. S.; Kang, H. C.; Lee, J. Y.; Lee, H. S.; Cho, Y. Y. Stat2 stability regulation: an intersection between immunity and carcinogenesis. *Experimental & molecular medicine* **2020**, *52* (9), 1526−1536.

https://doi.org/10.1021/acsnano.3c04726
ACS Nano 2023, 17, 14123−14135